Materials Advances

PAPER

View Article Online
View Journal | View Issue

Cite this: *Mater. Adv.*, 2022, 3, 665

Facile access to template-shape-replicated nitrogen-rich mesoporous carbon nanospheres for highly efficient CO_2 capture and contaminant removal†

Shashikant Shingdilwar, Subrata Dolui, Devendra Kumar and Sanjib Banerjee *

Received 28th September 2021,
Accepted 15th November 2021

DOI: 10.1039/d1ma00891a

rsc.li/materials-advances

Rising atmospheric CO_2 levels and water pollution have necessitated new research towards the development of novel CO_2 capture materials and innovative methods for wastewater treatment. Herein, we demonstrate a facile fabrication strategy to prepare novel template-shape-replicated nitrogen-rich mesoporous carbon nanospheres (NMCN) with high surface area, pore volume and ordered pore geometry *via* a combination of *in situ* co-condensation, surface-confined atom transfer radical polymerization (SC-ATRP) and post-polymerization modification. NMCN exhibited efficient CO_2 capture performance and contaminant removal capability from wastewater. This work may open a new direction for the design of novel porous nanomaterials for CO_2 capture and other emerging applications.

Introduction

The extensive combustion of fossil fuels in the post-industrial era to meet energy demands has resulted in a dramatic increase of the atmospheric concentration of CO_2. Atmospheric CO_2 concentration at present is ~400 ppm, which is expected to rise to 570 ppm by the year 2100. Due to this high level of atmospheric CO_2, various environmental issues have arisen, including global warming, imbalance in ocean acidification, unpredictable weather pattern and a slew of medical problems, including respiratory diseases.[1,2] The use of various renewable energy technologies on a large scale, such as solar, nuclear, and wind, has the potential to cut CO_2 emissions.[3] However, the replacement of fossil fuel sources with renewable energy in all applications is insufficient to mitigate CO_2's impact on climate change. As a result, there is an unmet demand to cut carbon emissions.[4] Post-combustion CO_2 capture from the source of the emission, such as power plants,[5] and geologic CO_2 storage,[6] which were once considered viable strategies, have gradually lost favor due to the high costs involved. To address this drawback, alternative CO_2 capture methods are urgently needed to combat climate change.[7–9] Various porous materials have been investigated to develop new CO_2 capture materials, such as zeolites,[10–13] carbon-based materials,[14–21] covalent organic frameworks,[22] metal organic frameworks,[23,24] polymers[25] and silica/polymer hybrids.[26–30] Porous carbon nanomaterials possessing controlled pore geometry and morphology are used in applications such as energy storage, catalysis, and air purification. Porous carbon is also employed as a CO_2 capture material.[17] However, the absence of ordered pore geometry in these materials has led to their poor CO_2 adsorption performance. Furthermore, the synthesis protocols of such materials involve stringent reaction conditions and multistep purification processes.

Mesoporous materials, with pore diameter between 2–50 nm and high surface area, organized pore geometry, and high pore volume, have received some interest due to their widespread use in adsorption, separation, catalysis, and sensing applications.[31] We hypothesized that nitrogen-rich functional mesoporous carbon nanospheres (NMCN) with high surface area and ordered pore geometry may be exploited to make efficient CO_2 capture materials. NMCN is synthesized *via* the surface-confined atom transfer radical polymerization (SC-ATRP)[32] of acrylonitrile (AN) and 4-vinylbenzyl chloride (VBC) from a bromo-functionalized mesoporous silica nanomaterial (MSN-Br), followed by carbonization and etching of the silica template.

Experimental section

Materials

Cetyltrimethylammonium bromide (CTAB, ≥96%, Aldrich), (3-aminopropyl)trimethoxysilane (APTMS, 97%, Aldrich), tetraethyl orthosilicate (TEOS, 98%, Aldrich), 2-bromo-2-methylpropionyl

Department of Chemistry, Indian Institute of Technology Bhilai, Raipur 492015, Chhattisgarh, India. E-mail: sanjib.banerjee@iitbhilai.ac.in

† Electronic supplementary information (ESI) available: Tables of results of the kinetic study. See DOI: 10.1039/d1ma00891a

bromide (BIBB, 98%, Aldrich), *N*,*N*,*N*′,*N*″,*N*″-pentamethyldiethylenetriamine (PMDETA, 99%, Aldrich), copper(I) chloride (CuCl, 97%, Aldrich), copper(II) chloride ($CuCl_2$, 97%, Aldrich), triethylamine (Et_3N, ≥99%, Aldrich), *N*-methyl-2-pyrrolidone (NMP, ≥99%, Aldrich), hydrogen fluoride (HF, 40%, Aldrich) and potassium hydroxide (KOH, Aldrich) were used as received. Acrylonitrile (AN, ≥99%, Aldrich) and 4-vinylbenzyl chloride (VBC, 90%, Aldrich) were purified by passing through a basic aluminium oxide (Aldrich) column to remove the inhibitor before use in polymerization. Xylene (Merck, India) was dried by refluxing over sodium/benzophenone just before use.

Preparation of amine-functionalized mesoporous silica nanoparticles

MSN-NH_2 was synthesized following an earlier reported procedure.[33] Typically, in a round-bottom flask, CTAB (1.0 g, 2.745 mmol), 2.0 M of aqueous NaOH (3.5 mL of 2.0 M, 7.0 mmol) and water (240 g, 13.335 mol) were mixed and heated for 30 min at 80 °C under stirring to obtain a clear solution. The pH of this solution was measured to be 12. Then, TEOS (4.67 g, 22.4 mmol) and APTMS (0.515 g, 2.875 mmol) were introduced rapidly to the solution under continuous magnetic stirring. A white precipitate appeared 5 min after the addition of TEOS and APTMS. The mixture was heated at 80 °C for another 2 h, then the product was isolated by hot filtration, washed with water/methanol, and dried under vacuum at 80 °C. CTAB template was eliminated by refluxing the crude product with a solution of 100 mL methanol and 1.0 mL of conc. HCl at 60 °C for 6 h. Then, the product was collected by filtration, washed with water/methanol, and dried under vacuum to obtain pure MSN-NH_2.

Preparation of bromo-initiator-functionalized mesoporous silica nanoparticles

MSN-Br was synthesized by the coupling reaction of MSN-NH_2 with 2-bromo-2-methylpropionyl bromide (BIBB). For a typical reaction, MSN-NH_2 was added to a flask, and TEA and dry CH_2Cl_2 were added to the flask under N_2 atmosphere. The flask was cooled to 0 °C, and BIBB was added to it dropwise at 0 °C under continuous magnetic stirring. After the addition, the temperature was raised to room temperature, and the reaction was allowed to continue at ambient temperature for another 12 h. After the reaction, the product was collected by filtration, washed successively with CH_2Cl_2 and acetone, and dried to obtain pure MSN-Br.

Calculation of initiator grafting density

Initiator grafting density (G_I) was calculated using TGA and eqn (1):

$$G_I = \frac{\dfrac{W_{\%\text{initiator+silica}}}{100 - W_{\%\text{initiator+silica}}} - \dfrac{W_{\%\text{silica}}}{100 - W_{\%\text{silica}}}}{M_{\text{initiator}} \times S_{sp}} \times N_A \ (\text{molecule nm}^{-2}) \quad (1)$$

where $W_{\%\text{initiator+silica}}$, $W_{\%\text{silica}}$, N_A, $M_{\text{initiator}}$ and S_{sp} stand for weight loss (between 120 °C to 800 °C) of the bromo-initiator-functionalized MSN-Br (= 16.4%), neat MSN (= 8.4%), Avogadro's number, molar mass of the initiator fragment after subtracting the molar mass of one Br atom (= 150 g mol^{-1}) and specific surface area of MSN-Br (= 1210 m^2 g^{-1}).

Preparation of –CH_2Cl functionalized mesoporous silica/polymer hybrid nanoparticles (MSPN)

MSPN was synthesized *via* SC-ATRP of AN/VBC from bromo-initiator-functionalized MSN-Br using the following molar ratio: $[AN + VBC]_0/[MSN\text{-}Br]_0/[CuCl]_0/[CuCl_2]_0/[PMDETA]_0$ = 200 : 1 : 1 : 0.1 : 1.1 at 70 °C for 24 h. In a typical polymerization, MSN-Br was added to a flask, which was evacuated at 60 °C for 2 h to eliminate any trapped gaseous entity or moisture. Then, a magnetic stir bar, degassed xylene, CuCl, $CuCl_2$ and PMDETA were introduced to the flask under N_2 atmosphere. Finally, degassed AN and VBC were added under N_2 flow, and the flask was heated at 790 °C. After polymerization, the crude product was isolated by centrifugation and washed successively with THF/methanol and finally dried to obtain the MSPN hybrid. For kinetics investigation of the polymerization, a series of polymerization reactions were performed, and these reactions were quenched at different polymerization times to monitor (i) %polymer grafting by TGA and (ii) the evolution of molecular weights and dispersities (by SEC) with time.

Preparation of nitrogen-rich mesoporous carbon nanospheres

Nitrogen-rich mesoporous carbon nanospheres (NMCN) were obtained *via* pyrolysis of the nitrogen-rich polymer (MSPN). Typically, the purified MSPN silica/polymer hybrid was first stabilized at 280 °C for 2 h under air flow at a heating rate of 1 °C min^{-1}, then purged with N_2 gas for 1 h and heated to reach 800 °C with a heating rate of 10 °C min^{-1}, then pyrolyzed at 800 °C for 6 h and finally cooled to ambient temperature. After carbonization, the silica template was selectively removed by HF, and the product was isolated by centrifugation and subsequently washed with water/ethanol, respectively, and then dried to obtain NMCN.

Characterization studies

X-Ray diffraction (XRD). XRD analysis of the prepared porous samples were carried out on a Bruker D8 Advance X-ray diffractometer equipped with a Cu X-ray tube (40 kV & 40 mA).

Attenuated total reflection infrared (ATR-IR) spectroscopy. IR spectra of the prepared porous samples were recorded using an IR spectrophotometer (PerkinElmer, Model: Spectrum 100) in the attenuated total reflectance (ATR) mode with a diamond crystal, using the spectral range of 4000–400 cm^{-1} and a resolution of 4 cm^{-1}.

Size exclusion chromatography (SEC). The silica-free cleaved polymer samples were analysed with an Agilent triple detection size exclusion chromatography (SEC) system equipped with two PL1113-6300 ResiPore 300 × 7.5 mm columns and using DMF as the eluent (at 35 °C, flow rate of 1 mL min^{-1}). The SEC instrument was calibrated using narrow linear poly(methyl methacrylate) standard samples.

Thermogravimetric analysis (TGA). TGA of the synthesized materials were performed using a Netzsch TG 209 F3 instrument (under air) from room temperature to 800 °C at a heating rate of 10 °C min^{-1}.

N_2 physisorption measurement. N_2 adsorption/desorption experiments of the porous materials were carried out using an Anton Paar (Model: Autosorb iQ-XR-XR-AG) gas sorption system at 77 K.

CO_2 capture characterization. CO_2 capture experiments of the synthesized porous carbon nanomaterials were carried out using an Anton Paar (Model: Autosorb iQ-C-AG) gas sorption analyzer system at 25 °C.

Field emission scanning electron microscopy (FESEM). The morphologies of the porous samples were analysed using a Zeiss Gemini SEM500 electron microscope at an accelerating voltage of 5 kV.

Dynamic light scattering (DLS). Hydrodynamic diameters (D_h) of the ethanol dispersions of porous samples were analysed using a Malvern particle size analyzer (Zetasizer NANO ZS90).

UV-vis absorption spectra. UV-vis absorption spectra of the solution of Coumarin 102 (C102) and suspension of C102-encapsulated NMCN were acquired in a Shimadzu UV-2600 spectrophotometer. %Encapsulation was calculated using the following eqn (2):

$$\%\text{Encapsulation} = \frac{\text{Absorbance}_{t=0} - \text{Absorbance}_{t=t}}{\text{Absorbance}_{t=0}} \times 100 \quad (2)$$

Photoluminescence spectra. Photoluminescence (PL) spectra of the samples were recorded in a Fluorolog FL3-211 (HORIBA Scientific) with a 450 Watt Xenon arc lamp.

Fluorescence microscopy. A drop of the dye-encapsulated nanomaterial sample suspension was placed on a glass slide, and images were recorded using a light microscope (DM2700M, Leica).

Results and discussion

Synthesis and structural characterization of the nitrogen-rich mesoporous carbon nanoparticles (NMCN)

Tertiary alkyl bromide-functionalized MSN-Br, suitable for use as ATRP initiator,[34,35] was synthesized *via* the process described in Scheme 1. First, -NH_2-functionalized MSN (MSN-NH_2) was synthesized *via in situ* co-condensation of TEOS and APTMS using CTAB as the template and with subsequent elimination of the CTAB template.[33,36] MSN-NH_2 was then coupled with 2-bromoisobutyryl bromide (BIBB) to introduce tertiary alkyl bromide-containing ATRP initiation sites (MSN-Br).[37] The ATR-IR spectrum of MSN-Br (Fig. 1a and Fig. S1, ESI†) exhibited characteristic bands at 2927 cm^{-1} (C–H asymm stretch.), 1060 cm^{-1} (Si–O–Si linkage)[32] and 614 cm^{-1} (C–Br stretch.).[38] This indicates that integration of the bromo-initiator functionality into the pore walls of the silica framework was successful. The significant weight loss (16.4%) of MSN-Br between 120 and 800 °C was attributed to the organic (aminopropyl + 2-bromoisobutyryl) functionalities, while the modest weight loss (8.4%) of neat MSN (Fig. 1b) is due to removal of water or other adsorbed gases. The initiator grafting density (G_I) of MSN-Br, estimated using eqn (1),[39] was found to be 0.33 molecule nm^{-2}. A high-intensity (100) reflection peak at $2\theta = 2.55°$ was observed

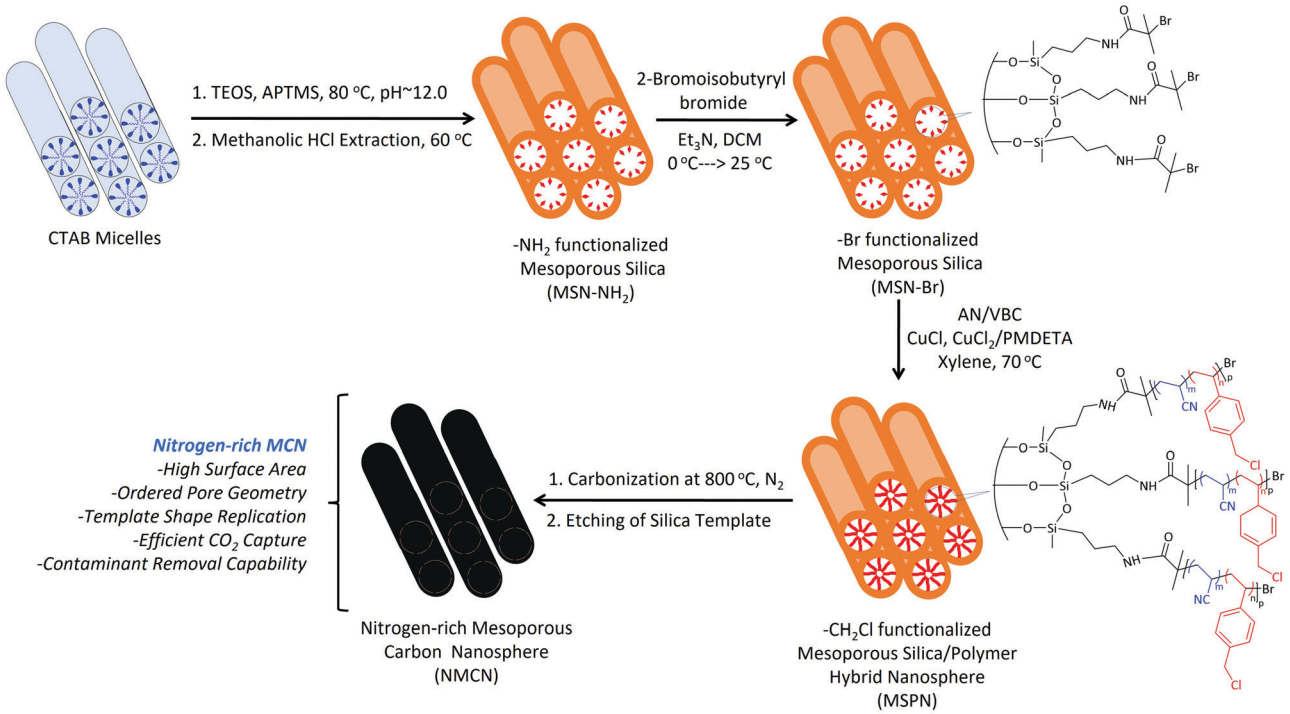

Scheme 1 Synthesis of nitrogen-rich mesoporous carbon nanoparticles.

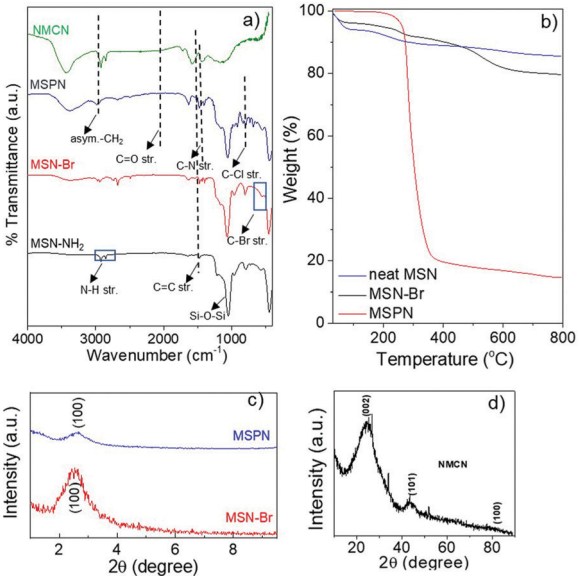

Fig. 1 Characterization of the obtained porous MSN-Br, MSPN and NMCN nanomaterials: (a) ATR-IR spectra, (b) TGA thermograms and (c and d) powder XRD patterns.

in the XRD pattern of MSN-Br (Fig. 1c), suggesting the presence of cylindrical mesopores.[33]

N_2 sorption analyses of MSN-Br (Fig. 2a) revealed a high specific surface area (S_{BET}) of 1210 m^2 g^{-1} and narrow pore size distribution (PSD) with an average diameter of around 1.98 nm and pore volume of 0.728 cc g^{-1}, suggesting a cylindrical mesoporous structure.[33] MSN-Br exhibited spherical morphology diameters ranging from 200–280 nm, as revealed by the FESEM image (Fig. 3). Somewhat higher value (344 nm) of the MSN-Br diameter was obtained from dynamic light scattering (DLS) compared to that from FESEM, which is most likely due to MSN-Br's hydrodynamic nature.[40]

Subsequent SC-ATRP of acrylonitrile (AN) in the presence of a functional monomer, 4-vinylbenzyl chloride (VBC, 5, 10 and 15 mol%), from MSN-Br using CuCl/$CuCl_2$/PMDETA led to the synthesis of MSPN silica/polymer hybrids. FTIR spectrum of a representative MSPN hybrid (Fig. 1a) showed bands at 1060 (Si–O–Si linkage), 1589 (–N–C═O band of PAN),[41] and 1415 (–C═N band of PAN),[41] along with additional bands at 1474, 1512 and 1626 (stretching vibration of the phenyl ring),[42] 827 (CH_2 of chloromethyl functionality),[43] and 725 cm^{-1} (C–Cl stretching vibration). A representative MSPN hybrid (with 15% –CH_2Cl functionalization) revealed 66% polymer grafting into the MSN, as revealed by TGA analysis (Fig. 1b).

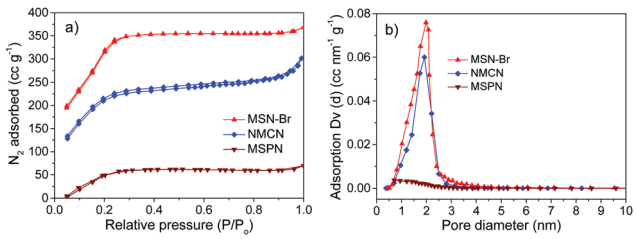

Fig. 2 (a) N_2 adsorption–desorption isotherm and (b) pore size distribution of porous MSN-Br, MSPN and NMCN nanomaterials.

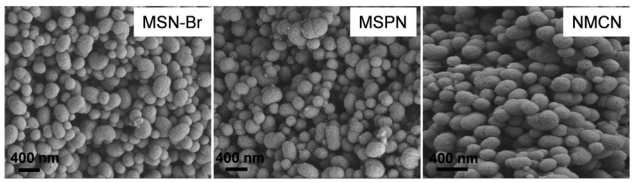

Fig. 3 FESEM images of porous MSN-Br, MSPN and NMCN nanomaterials.

XRD analysis of a representative MSPN-15% hybrid (Fig. 1c) exhibited a diffraction peak at $2\theta = 2.58^{\circ}$, although with lower intensity compared to that of MSN-Br. This suggests polymer grafting of the mesopores of MSN-Br. The S_{BET} of MSPN reduced to 94 m^2 g^{-1} from that of the starting material, MSN-Br (S_{BET} = 1210 m^2 g^{-1}), during which the total pore volume also shrunk to 0.041 from 0.728 cc g^{-1} (Fig. 2 and Table 1). Spherical morphology of the MSN-Br template remained intact in MSPN-15% even after polymer grafting, as revealed by FESEM analysis.

To have a better idea of the surface grafting of the polymer, a detailed kinetic investigation was carried out (see Experimental section for more details, Table S1, ESI†), and the evolution of %polymer grafting (from the TGA analysis) and molar masses/dispersities with time (by SEC analysis) was monitored. The %polymer grafting into the mesoporous channel of MSN-Br increased steadily with time, reaching 66% after 24 h of polymerization. The molar mass of the cleaved polymer (after dissolution of the silica template) increased linearly with conversion (Fig. 4b and Table S1, ESI†), sustaining low $Đ$ values (1.17–1.25) during polymerization (Fig. 4b), indicating a controlled copolymerization.[35,44–46]

Mesoporous carbon nanospheres (MCN) were obtained by a two-step thermal treatment[47,48] involving thermal stabilization (under air) and carbonization (under N_2) of the MSPN silica/polymer hybrids, followed by removal of silica template. The FTIR spectrum of NMCN (Fig. 1a) exhibits characteristic bands at ~1626 (C═C stretching), ~2920 (CH_2 asymm stretch.) and 2847 cm^{-1} (CH_2 symm stretch.), which originate from the adsorbed gaseous AN monomer fragments produced during pyrolysis.[49] Notably, the absence of the Si–O–Si absorption band in the IR spectrum of NMCN suggests complete dissolution of the

Table 1 Molecular characterization data of different mesoporous nanoparticles

Entry	Material	D_{SEM}[a] (nm)	D_h[b] (nm)	S_{BET}[c] (nm)	Total pore volume[c]	Pore diameter[c]
E1	MSN-Br	200–280	344	1210	0.728	1.98
E2	MSPN	196–240	292	94	0.041	—[d]
E3	NMCN	190–260	310	860	0.462	1.92

[a] Diameter measured from FESEM. [b] Hydrodynamic diameter measured from DLS. [c] Analysed by N_2 adsorption/desorption study. [d] Pores were inaccessible to N_2 adsorbate.

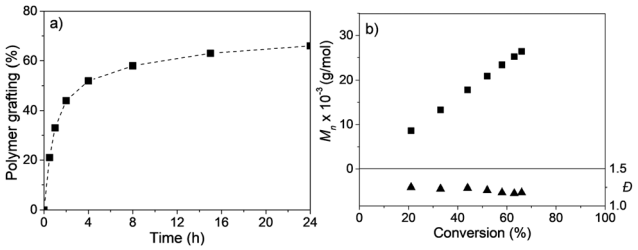

Fig. 4 (a) Evolution of %polymer grafting into the mesopores of MSN-Br *vs.* time and (b) plot of M_n and $Đ$ of the cleaved polymer *vs.* %polymer grafting for SC-ATRP of AN + 15% VBC in xylene at 90 °C.

silica framework. The XRD pattern (Fig. 1d) of NMCN showed broad peaks at 2θ of 25°, 44°, and 80° ascribed to the (002), (101), and (100) reflections of a typical graphitic carbon-type structure.[32]

The S_{BET} of NMCN was estimated to be 860 m^2 g^{-1}, and the average pore diameter of 1.92 nm and total pore volume of 0.462 cc g^{-1} (Table 1) were estimated from the N_2 sorption analysis. Notably, this high pore diameter and pore volume of NMCN are key features for its potential application as adsorbent. The FESEM image of NMCN (Fig. 3) reveals it has retained the spherical morphology of MSN-Br (Table 1). The formation of spherical mesoporous NMCN, retaining the morphology of the MSN, was mainly enabled by the presence of the interconnected mesoporous network in the material and high polymer grafting into the mesopores of MSN-Br *via* SC-ATRP.[50] The diameters of NMCN obtained from DLS are somewhat higher than D_{FESEM}. This is probably due to their hydrodynamic nature and aggregation in ethanol.

CO_2 is an anthropogenic greenhouse gas and is majorly accountable for global warming.[20,51,52] The synthesized mesoporous NMCN nanoparticles were employed as potential candidates for CO_2 capture. CO_2 adsorption performance at 25 °C (Fig. 5) of the three porous NMCN nanoparticle samples bearing 5, 10 and 15% functionalization exhibited acceptable CO_2 adsorption capacities of 2.84, 3.76 and 4.93 mmol g^{-1}, respectively. These results are comparable to the reported porous N-rich carbon nanospheres, including copolymer-templated nitrogen-enriched porous nanocarbon,[20] N-doped acicular hollow porous carbon,[53] porous carbon derived from sugarcane[54] and porous carbon derived from sustainable biomass.[55] Among

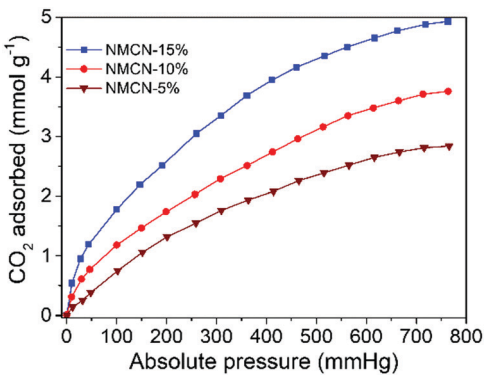

Fig. 5 CO_2 adsorption isotherms for NMCN samples at 25 °C.

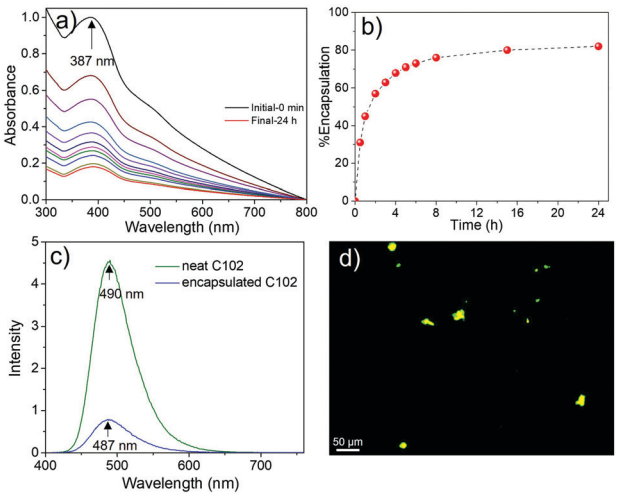

Fig. 6 (a) Time-dependent (initial – 0 min, final – 24 h) UV-Vis spectra of C102 after incubating with NMCN; (b) evaluation of %encapsulation of C102 with time; (c) fluorescence emission spectra of aqueous solution of C102 and aqueous suspension of C102 encapsulated-NMCN (Excitation wavelength: 390 nm); (d) fluorescent microscopy images of C102 encapsulated-NMCN.

the three samples, NMCN (15%) displays the highest CO_2 adsorption, possibly due to higher pore volume.

The efficiency of NMCN for the removal of a representative hydrophobic dye (Coumarin 102, C102) from water was tested, and the encapsulation capacity was observed by UV-Vis spectroscopy. The absorbance of C102 at 387 nm decreased gradually with time (Fig. 6a), leading to ~82% dye exchange after incubation for 24 h (Fig. 6b). The fluorescence emission spectrum of NMCN (Fig. 6c) with encapsulated C102 was of lower intensity than that of neat C102; however, the peak position remains same, suggesting successful dye encapsulation. Furthermore, the fluorescence light microscopic image (Fig. 6d) depicts green light-emitting beads of NMCN with encapsulated C102, confirming successful encapsulation of the dye inside the mesopores of NMCN.

Conclusions

In summary, this work demonstrates, for the very first time, the development of a facile fabrication method for nitrogen-rich mesoporous carbon nanomaterials (NMCN) with high surface area and ordered pore geometry for efficient ambient-temperature CO_2 capture and contaminant removal. Overall, the CO_2 uptake performance of NMCN is comparable to or better than the contemporary benchmark porous materials, including carbons, zeolites, and metal organic frameworks. This approach, with (i) greater sustainability, including but not limited to carbon neutrality, and (ii) simpler and cost-effective preparation routes, leading to the preparation of nitrogen-rich mesoporous carbon nanomaterials with improved properties for specific applications in CO_2 capture and contaminant removal, introduces a new avenue for the fabrication of unique advanced porous materials for a wide

range of potential applications in adsorption, energy, catalysis, and medicine.

Conflicts of interest

There are no conflicts to declare.

Acknowledgements

We acknowledge grants from SERB, Govt. of India, under Ramanujan Fellowship Award (SB/S2/RJN-113/2016) and IIT Bhilai under Research Initiation Grant. We thank Arindam Mondal for his help on the PL measurement. SS and DK thank DBT, Govt. of India and CSIR, Govt. of India for their fellowship.

Notes and references

1 S. Chu, *Science*, 2009, **325**, 1599.
2 A. Harjanne and J. M. Korhonen, *Energy Policy*, 2019, **127**, 330–340.
3 C. W. Forsberg, *Prog. Nucl. Energy*, 2009, **51**, 192–200.
4 M. Bui, C. S. Adjiman, A. Bardow, E. J. Anthony, A. Boston, S. Brown, P. S. Fennell, S. Fuss, A. Galindo, L. A. Hackett, J. P. Hallett, H. J. Herzog, G. Jackson, J. Kemper, S. Krevor, G. C. Maitland, M. Matuszewski, I. S. Metcalfe, C. Petit, G. Puxty, J. Reimer, D. M. Reiner, E. S. Rubin, S. A. Scott, N. Shah, B. Smit, J. P. M. Trusler, P. Webley, J. Wilcox and N. Mac Dowell, *Energy Environ. Sci.*, 2018, **11**, 1062–1176.
5 A. Samanta, A. Zhao, G. K. H. Shimizu, P. Sarkar and R. Gupta, *Ind. Eng. Chem. Res.*, 2012, **51**, 1438–1463.
6 M. D. Zoback and S. M. Gorelick, *Proc. Natl. Acad. Sci. U. S. A.*, 2012, **109**, 10164–10168.
7 K. S. Lackner, S. Brennan, J. M. Matter, A.-H. A. Park, A. Wright and B. van der Zwaan, *Proc. Natl. Acad. Sci. U. S. A.*, 2012, **109**, 13156–13162.
8 E. S. Sanz-Pérez, C. R. Murdock, S. A. Didas and C. W. Jones, *Chem. Rev.*, 2016, **116**, 11840–11876.
9 K. Z. House, A. C. Baclig, M. Ranjan, E. A. van Nierop, J. Wilcox and H. J. Herzog, *Proc. Natl. Acad. Sci. U. S. A.*, 2011, **108**, 20428–20433.
10 P. Subha, B. N. Nair, V. Visakh, C. Sreerenjini, A. P. Mohamed, K. Warrier, T. Yamaguchi and U. Hareesh, *J. Mater. Chem. A*, 2018, **6**, 7913–7921.
11 A. Maity, R. Belgamwar and V. Polshettiwar, *Nat. Protoc.*, 2019, **14**, 2177–2204.
12 M. Niu, H. Yang, X. Zhang, Y. Wang and A. Tang, *ACS Appl. Mater. Interfaces*, 2016, **8**, 17312–17320.
13 N. Minju, B. N. Nair, A. Peer Mohamed and S. Ananthakumar, *Sep. Purif. Technol.*, 2017, **181**, 192–200.
14 Z. Zhang, Z. P. Cano, D. Luo, H. Dou, A. Yu and Z. Chen, *J. Mater. Chem. A*, 2019, **7**, 20985–21003.
15 H. He, W. Li, M. Zhong, D. Konkolewicz, D. Wu, K. Yaccato, T. Rappold, G. Sugar, N. E. David and K. Matyjaszewski, *Energy Environ. Sci.*, 2013, **6**, 488–493.
16 Z. Li, D. Wu, X. Huang, J. Ma, H. Liu, Y. Liang, R. Fu and K. Matyjaszewski, *Energy Environ. Sci.*, 2014, **7**, 3006–3012.
17 J. Zhang, R. Yuan, S. Natesakhawat, Z. Wang, Y. Zhao, J. Yan, S. Liu, J. Lee, D. Luo, E. Gottlieb, T. Kowalewski, M. R. Bockstaller and K. Matyjaszewski, *ACS Appl. Mater. Interfaces*, 2017, **9**, 37804–37812.
18 W. Shen, S. Zhang, Y. He, J. Li and W. Fan, *J. Mater. Chem.*, 2011, **21**, 14036–14040.
19 M. Nandi, K. Okada, A. Dutta, A. Bhaumik, J. Maruyama, D. Derks and H. Uyama, *Chem. Commun.*, 2012, **48**, 10283–10285.
20 M. Zhong, S. Natesakhawat, J. P. Baltrus, D. Luebke, H. Nulwala, K. Matyjaszewski and T. Kowalewski, *Chem. Commun.*, 2012, **48**, 11516–11518.
21 Y. K. Kim, G. M. Kim and J. W. Lee, *J. Mater. Chem. A*, 2015, **3**, 10919–10927.
22 Y. Zeng, R. Zou and Y. Zhao, *Adv. Mater.*, 2016, **28**, 2855–2873.
23 Y. Chen, Z. Qiao, J. Huang, H. Wu, J. Xiao, Q. Xia, H. Xi, J. Hu, J. Zhou and Z. Li, *ACS Appl. Mater. Interfaces*, 2018, **10**, 38638–38647.
24 M. Ding, R. W. Flaig, H.-L. Jiang and O. M. Yaghi, *Chem. Soc. Rev.*, 2019, **48**, 2783–2828.
25 F.-Q. Liu, L.-L. Wang, G.-H. Li, W. Li and C.-Q. Li, *ACS Appl. Mater. Interfaces*, 2017, **9**, 33997–34004.
26 A. Holewinski, M. A. Sakwa-Novak and C. W. Jones, *J. Am. Chem. Soc.*, 2015, **137**, 11749–11759.
27 R. Zhang, X. Wang, S. Liu, L. He, C. Song, X. Jiang and T. P. Blach, *ACS Appl. Mater. Interfaces*, 2019, **11**, 36515–36524.
28 A. R. Sujan, S. H. Pang, G. Zhu, C. W. Jones and R. P. Lively, *ACS Sustainable Chem. Eng.*, 2019, **7**, 5264–5273.
29 F. Lou, A. Zhang, G. Zhang, L. Ren, X. Guo and C. Song, *Appl. Energy*, 2020, **264**, 114637.
30 M. L. Sarazen, M. A. Sakwa-Novak, E. W. Ping and C. W. Jones, *ACS Sustainable Chem. Eng.*, 2019, **7**, 7338–7345.
31 J. Wang, Q. Ma, Y. Wang, Z. Li, Z. Li and Q. Yuan, *Chem. Soc. Rev.*, 2018, **47**, 8766–8803.
32 S. Banerjee, T. K. Paira, A. Kotal and T. K. Mandal, *Adv. Funct. Mater.*, 2012, **22**, 4751–4762.
33 S. Huh, J. W. Wiench, J.-C. Yoo, M. Pruski and V. S.-Y. Lin, *Chem. Mater.*, 2003, **15**, 4247–4256.
34 K. Matyjaszewski, *Macromolecules*, 2012, **45**, 4015–4039.
35 K. Matyjaszewski and J. Xia, *Chem. Rev.*, 2001, **101**, 2921–2990.
36 P. Mondal, S. Banerjee, A. S. Roy, T. K. Mandal and S. M. Islam, *J. Mater. Chem.*, 2012, **22**, 20434–20442.
37 J. Pyun, S. Jia, T. Kowalewski, G. D. Patterson and K. Matyjaszewski, *Macromolecules*, 2003, **36**, 5094–5104.
38 G. Mukherjee and K. Biradha, *CrystEngComm*, 2014, **16**, 4701–4705.
39 M. Save, G. Granvorka, J. Bernard, B. Charleux, C. Boissière, D. Grosso and C. Sanchez, *Macromol. Rapid Commun.*, 2006, **27**, 393–398.
40 Q. Zeng, D. Wu, C. Zou, F. Xu, R. Fu, Z. Li, Y. Liang and D. Su, *Chem. Commun.*, 2010, **46**, 5927–5929.

41 X. Zhang, H. Qin, X. Zheng and W. Wu, *Mater. Res. Bull.*, 2013, **48**, 3981–3986.
42 C. Valencia, C. H. Valencia and F. Zuluaga, *Molecules*, 2018, **23**, 2651.
43 N. D. Koromilas, G. C. Lainioti, E. K. Oikonomou, G. Bokias and J. K. Kallitsis, *Eur. Polym. J.*, 2014, **54**, 39–51.
44 A. Saha, T. K. Paira, M. Biswas, S. Jana, S. Banerjee and T. K. Mandal, *J. Polym. Sci., Part A: Polym. Chem.*, 2015, **53**, 2313–2319.
45 S. Banerjee, V. Ladmiral, A. Debuigne, C. Detrembleur, S. M. W. Rahaman, R. Poli and B. Ameduri, *Macromol. Rapid Commun.*, 2017, **38**, 1700203.
46 S. Banerjee, Y. Patil, O. Gimello and B. Ameduri, *Chem. Commun.*, 2017, **53**, 10910–10913.
47 C. Tang, L. Bombalski, M. Kruk, M. Jaroniec, K. Matyjaszewski and T. Kowalewski, *Adv. Mater.*, 2008, **20**, 1516–1522.
48 M. Zhong, E. K. Kim, J. P. McGann, S.-E. Chun, J. F. Whitacre, M. Jaroniec, K. Matyjaszewski and T. Kowalewski, *J. Am. Chem. Soc.*, 2012, **134**, 14846–14857.
49 D. S. Achilias, *Eur. Polym. J.*, 2007, **43**, 2564–2575.
50 D.-W. Wang, F. Li, M. Liu, G. Q. Lu and H.-M. Cheng, *Angew. Chem., Int. Ed.*, 2008, **47**, 373–376.
51 G.-P. Hao, W.-C. Li, D. Qian and A.-H. Lu, *Adv. Mater.*, 2010, **22**, 853–857.
52 N. P. Wickramaratne and M. Jaroniec, *J. Mater. Chem. A*, 2013, **1**, 112–116.
53 X. He, J. Liu, Y. Jiang, M. Yaseen, H. Guan, J. Sun, X. Cui, D. Liao and Z. Tong, *Chem. Eng. J.*, 2019, **361**, 278–285.
54 S. O. Adio, S. A. Ganiyu, M. Usman, I. Abdulazeez and K. Alhooshani, *Chem. Eng. J.*, 2020, **382**, 122964.
55 P. Yang, L. Rao, W. Zhu, L. Wang, R. Ma, F. Chen, G. Lin and X. Hu, *Ind. Eng. Chem. Res.*, 2020, **59**, 6194–6201.